Multibody System Dynamics
https://doi.org/10.1007/s11044-026-10185-2

RESEARCH

# An innovative wheel rail wear model under conformal contact conditions

Francesco Distaso[1] · Leandro Nencioni[1] · Alessio Cascino[1] · Enrico Meli[1] · Andrea Rindi[1]

Received: 21 November 2025 / Accepted: 24 July 2026


**Abstract**
Wear at the wheel–rail interface is a key factor affecting vehicle safety, dynamics, and maintenance strategies. The progressive modification of wheel and rail profiles due to wear can significantly influence stability, comfort, and operating costs, making accurate prediction of profile evolution essential. Traditional wear models often rely on simplified flat-contact assumptions, such as those in the FASTSIM algorithm, which fail to capture the real behavior under conformal contact conditions typical of worn surfaces, curves, and flange–rail interactions. This study proposes a wear model integrating a conformal contact formulation by extending the Kik–Piotrowski normal contact model with Blanco–Lorenzo's coefficients and enhancing FASTSIM to handle non-elliptical and curved patches in the tangential problem. Implemented within a Simpack Rail multibody framework, the model reproduces realistic operating conditions. Comparisons with conventional non-conformal models highlight that the proposed approach achieves a superior balance between computational efficiency and physical accuracy, providing a more reliable tool for wear prediction and maintenance optimisation in railway systems.

**Keywords** Wheel-rail contact · Conformal contact · Multibody dynamic simulation · Wear model · Conformity

## 1 Introduction

Wear is one of the most important mechanisms affecting the life of both wheels and rails, for this reason wear becomes one of the most important objects of study and research. The goal is to predict the evolution of wheel profiles during the time. Predicting these phenomena is fundamental for the security of railway vehicles, the vehicle's dynamics, and particularly, the development of a financially sustainable maintenance strategy. Wear at the wheel-rail interface progressively modifies the nominal profiles, with significant implications for vehicle stability, safety and comfort.

These aspects generally require the need for periodic reprofiling of wheel and rail profiles, for the wheel it's possible to perform a reprofiling procedure, a chip-removal machining process designed to redefine the original profile on a smaller rolling diameter, this

✉ Francesco Distaso
francesco.distaso@unifi.it

[1] DIEF Department of Industrial Engineering, University of Florence, Florence, Italy

operation is best performed on a pit lathe so as to minimize the risk of wheel stepping. If the reference tolerances are out of the acceptable range, defined into the European Normative, the operation of reprofiling procedure is not achievable and it is possible to change rims. Instead for the rail the reconstruction of the rail profile is carried out through a reprofiling procedure of a head of rail, otherwise it is possible to do “track renewal”, in which the railway track is replaced with a frequency that varies according to applications.

The wear model makes use of multibody simulation of railway vehicles, that needs a reliable contact model that satisfies some fundamental specifics such as:

- Accurate description of the global and local contact phenomena;
- General and robust treatment of the multiple contact;
- High numerical efficiency to be used in a complex multibody model;
- Compatibility with commercial multibody software (Simpack Rail, Adams Rail, etc.).

The wheel-rail contact problem has been extensively investigated, with numerous models proposed in the literature. Many of the models developed specifically for multibody simulation rely on key simplifying assumptions that allow the complex nature of wheel-rail interaction to be reduced to a form suitable for efficient numerical computation. One of the most common assumptions is that the contact patch is significantly smaller than the dimensions of the contacting bodies. This leads to the simplification of the contact area as flat, and the interacting bodies as elastic half-spaces. While this assumption holds true in many cases, it does not always reflect real-world operating conditions, in fact it is very common to have conformal contact conditions. For instance, when a railway vehicle negotiates a curve, the contact point on the outer wheel tends to shift towards the flange and the gauge corner of the rail. In such cases, the contact area is no longer flat but curved laterally. Similarly, wear may alter the wheel and rail profile surfaces, leading to an increasingly conformal contact patch, this demonstrates that another case where the planar contact hypothesis is not always valid in presence of worn surfaces. Even on straight tracks, worn surfaces may lead to conformal contact conditions, as profile degradation affects the interaction geometry. Moreover, in these conformal cases, the spin contributes due to the strongly warped geometry, which is large and causes large and severe abrasive wear phenomena [1, 2]. These effects can intensify abrasive wear mechanisms, leading to faster surface degradation. Given these considerations, it becomes evident that conventional flat-contact models may not be sufficient, and a more accurate conformal contact model should be adopted to better represent real operating conditions and wear behavior [3].

In literature are available some models [4–9], the most used for commercial software multibody is the FASTSIM algorithm [10], where the normal problem is solved using Hertz theory [11] and the tangential problem is solved by an iterative strip algorithm. This solution is based on hypothesis such as flat and elliptical contact patch, for this reason the FASTSIM algorithm is not recommended in presence of conformal contact conditions. It is possible to use also a model available in literature that is CONTACT algorithm [12–14] by Kalker, which is however computationally expensive. Furthermore, another class of conformal contact models is available in the literature [15, 16]. An alternative solution for general flat contact conditions is the Kik-Piotrowski algorithm [17].

To address these challenges, this study presents a new reliable wear model integrating a conformal contact model [3] that captures the effects of conformity while ensuring an optimal compromise between computational efficiency and accuracy. The normal component of the contact problem extends the Kik-Piotrowski contact model [17] using Blanco-Lorenzo’s coefficients [18]. Additionally, the tangential component of the contact model extends the FASTSIM algorithm to accommodate non-elliptical and curved contact patches. The newly

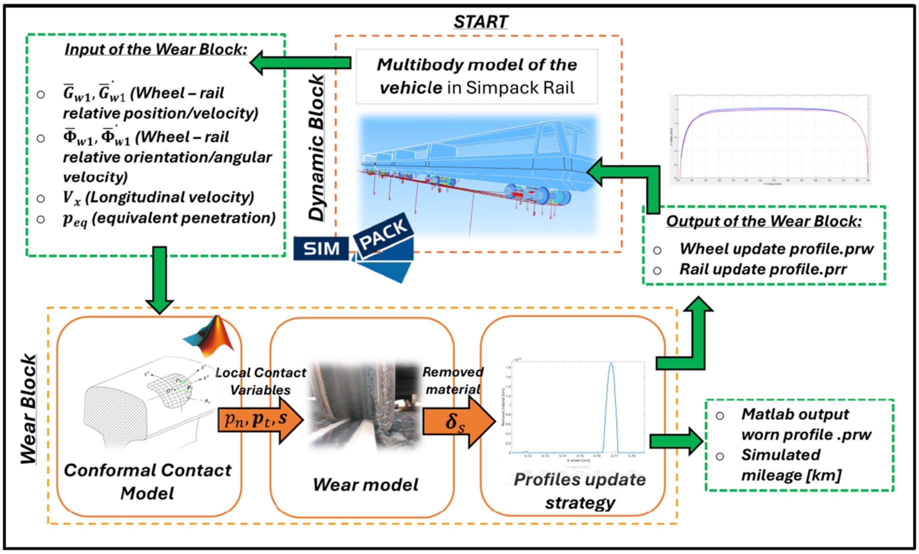


**Fig. 1** Architecture of the model

developed wear model is then implemented into multibody model, developed into Simpack Rail, to reproduce a real railway scenario with realistic operating conditions, and to obtain the simulated worn wheel profiles. The worn wheel profiles predicted by the new model are compared with those obtained from a wear model based on a non-conformal contact model. In particular, the wheel profile evolution, geometries and associated dimensional parameters are analysed, so as to assess the influence on the evolution of wheel profile in conformal contact conditions as opposed to non-conformal contact.

Finally, while the numerical robustness and computational stability of the proposed methodology are thoroughly verified throughout the simulated scenarios, a systematic parameter sensitivity analysis, such as evaluating the specific effects of variations in the friction coefficient or the material elastic modulus, falls outside the scope of this paper and represents a dedicated topic for future research.

## 2 Architecture of the model

As it is possible to see in Fig. 1, the present model is composed of two blocks: the dynamic block that includes the multibody model of the simulated vehicle, and the wear block.

The dynamic block is composed by multibody model of the vehicle, developed in Simpack Rail. During the dynamic simulations, at each temporal step, the multibody model provides the following kinematics variables, as shown in Fig. 2:

- spatial position of the wheelset within the auxiliary reference system;
- orientation of the wheelset within the auxiliary reference system;
- spatial velocity of the wheelset within the auxiliary reference system;
- rotational velocity of the first wheelset within the auxiliary reference system.

The co-simulation solver available in Simpack Rail enables interaction between the multibody model and the Wear block. These variables are provided as input to one of the

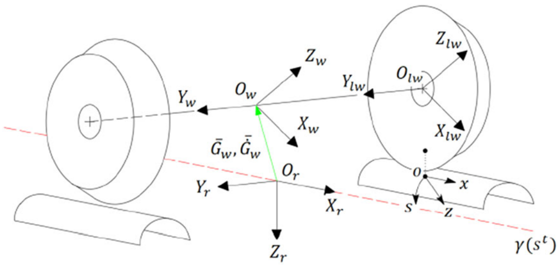


**Fig. 2** Input variables of conformal contact model

three sub-blocks of the wear block, specifically the conformal contact model component, developed in MATLAB/Simulink.

The conformal contact model is composed of two main modules, the normal problem function and the tangential problem function. The kinematics variables are given as input to the normal problem function, which is able to evaluate the position and number of the geometrical contact points, the rigid penetration of the bodies $\delta$, and finally the rigid penetration area $A_{rp}$. Based on these variables, the model can evaluate the real contact area $A_c$ for each geometrical contact point. These variables are the fundamental inputs of the normal contact problem which is an extension of the Kik-Piotrowski contact model [19, 20].

Starting from the global variables of the wheelset under investigation, that is global position $G_w$, the orientation $\phi_w$ and their respective time derivatives $\dot{G}_w$, $\dot{\phi}_w$ with respect to the auxiliary reference frame, a dedicated contact search algorithm has been implemented in MATLAB/Simulink. This algorithm, developed by the authors as a trade-off between computational efficiency and accuracy (since contact search is typically one of the most demanding parts of a contact model), delivers key outputs such as: the virtual penetration area $A_{rp}$, the rigid penetration $\delta$, the actual contact area $A_c$ and the position of the corresponding i-th geometrical contact point. These results are then provided as input to the normal-contact function of the proposed model, which is responsible for determining the pressure distribution $p_n$, as well as the resulting normal forces $F_n$ and moment $M_n$.

Thereafter, these outputs are passed to the second main function of the conformal contact model, the tangential function. This function is based on an extended version of the FASTSIM algorithm [10], capable of handling non-flat and non-elliptical patches via the KBTNH procedure [21]. Its inputs include the real contact area $A_c$, the pressure distribution $p_n$ obtained from the normal function, together with the global velocities $\dot{G}_w$, $\dot{\phi}_w$ supplied by the vehicle's multibody model shown in Fig. 3. Based on these quantities, the tangential block evaluates the local contact parameters: tangential pressure distribution $p_t$, local sliding components $s$, adhesion regions $A_{adh}$ and sliding regions $A_{sld}$ within the contact patch. From a global perspective, the block integrates the tangential pressure distribution over the contact area, thus obtaining the global tangential forces $F_n$ and moment $M_n$, which are then transferred back as inputs to the multibody vehicle model and applied to the wheelset.

Finally, as shown in Fig. 1, the outputs of the conformal contact model for each contact patch are:

- From a local point of view:
  - The normal and tangential pressure distributions $p_n$, $p_t$;
  - The components of local sliding $s$;
  - The contact patch area $A_c$;
  - The adhesion and sliding areas $A_{adh}$, $A_{sld}$.
- From a global point of view:

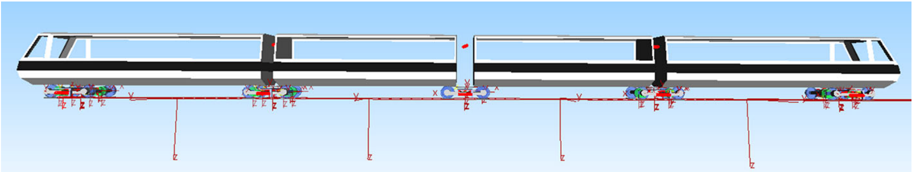

**Fig. 3** Multibody model of railway vehicle

- The components of the normal and tangential forces, resulting from the integration procedure of the normal and tangential pressure distributions defined in the auxiliary reference system;
- The components of the normal and tangential torques, resulting from the integration procedure of the normal and tangential pressure distributions defined in the auxiliary reference system.

The wear model employs an energetic approach, the first step is to calculate the Wear Index, that is the frictional power generated by the tangential contact pressure distribution, which is fundamental to determining the distribution of removed material. Lewis's law is then applied to find the distribution of removed material, that correlates the Wear Index $I_w$ to Wear Rate $K_r$. There are three wear regimes: mild, severe and catastrophic. Finally, from the Wear model it is possible to obtain the removed material $\delta_s$ and then with these parameters, the wheel worn profile is generated from the original profile through an innovative profile update strategy. The update strategy is composed by four different sections: longitudinal integration, track integration, sum of the contact points contributes and the scaling of the results. The Wear block provides to generate the wheel worn profile file .prw, that is the new input of the multibody model. At this point, the cycle is completed, and the model restarts to generate subsequent wheel worn profile.

## 3 The multibody model of railway vehicle

The present section describes the vehicle model used as a test case for the multibody simulations. The selected benchmark is an Italian metropolitan vehicle. The multibody model is built in Simpack Rail environment, it is a vehicle with locked composition and consist of four carbody and ten wheelsets distributed on two traditional bogies on the top and on the bottom of the train and three intermediate bogies with Jacobs-type architecture. The wheel profile adopted in the simulations is the ORE S1002, interacting with a UIC 50 rail profile canted at 1/20.

This multibody model comprises a set of rigid bodies interconnected through constraints and force elements, such as springs and dampers. For example, the suspensive stages of this multibody model are modelled by means of three-dimensional viscoelastic force element considering all the mechanical non linearities of system (bumpstop clearance, dampers, etc.).

The other engineering characteristics of the vehicle and the track are summarized in the Table 1.

**Table 1** Main characteristics of vehicle and track

| | |
|---|---|
| Total vehicle length | 49,000 mm |
| Max width | 2650 mm |
| Bogie centre distance | 10,850 – 11,000 – 11,000 – 10,850 mm |
| Motor and trailer bogie wheelbase | 2000 mm |
| Wheel diameter | 711 mm |
| Track gauge | 1435 mm |
| Rail profile | UIC 50 |
| Rail cant | 1/20 |

## 4 Conformal contact model

### 4.1 Normal problem

The normal problem of the contact model is based on an extension of the Kik-Piotrowski contact model [17], which is relied on the fundamental assumption that the real shape of the contact bodies in the contact patch is neglected and approximated through two elastic half-spaces (Fig. 4).

Following this hypothesis, the normal contact pressure distribution $p_n(x, y)$ is correlated to the displacements along the vertical axis $w(x, y)$ by means the influence function of Cerruti-Bussinesq.

$$w\left(x, y\right) = \frac{1-\upsilon^2}{\pi E}\int_{A_c}\frac{p_n\left(x', y'\right)}{\sqrt{(x-x')^2+(y-y')^2}}dA_c = \int_{A_c} B_{nn_{conf}} \cdot p_n\left(x', y'\right)dA_c \tag{1}$$

According to Blanco-Lorenzo's method [18], the influence coefficients for conformal geometries are approximated through a combination of the influence coefficients of the half-spaces, but the extension of Kik-Piotrowski model requires only a single corrected influence coefficient, namely $B_{nn_{conf}}$.

$$B_{nn_{conf}} \approx B_{nn} \cdot \cos\left(\alpha\right) - B_{nt} \cdot \sin\left(\alpha\right) \tag{2}$$

In general, an influence coefficient $B_{ij}$ represents the parameter that link the displacement in direction $i$ of a point $I$ in an elastic half-space to the load applied at a point $J$ of another elastic half-space in direction $j$. $B_{nn}$ and $B_{nt}$ are the influence coefficients introduced by Kalker. In this way, developing the calculation, it is possible to obtain a new influence function that is applicable in conformal contact conditions:

$$w\left(x, y\right) = \frac{1+\upsilon}{\pi E}\int_{A_c}\left(\frac{p_n\left(x', y'\right)\cos\left(\alpha\right)\left(1-\upsilon\right)}{\sqrt{(x-x')^2+(y-y')^2}} + \frac{p_n\left(x', y'\right)\sin\left(\alpha\right)Ky}{(x-x')^2+(y-y')^2}\right)dA_c \tag{3}$$

In case of conformal contact, it is fundamental to consider the conformity effect and the surface curvature, for this reason a change of coordinates must be performed. Therefore, to develop an efficient and reliable model when the contact patch is non-flat and non-small with respect to the curvature radii of the contacting bodies, it is important to change coordinates with the following variables:

$$\begin{cases} x \rightarrow x^r \\ y \rightarrow s^r \end{cases} \tag{4}$$

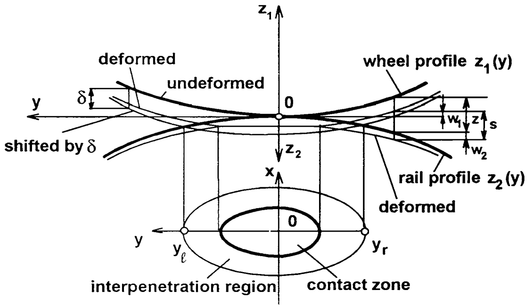


**Fig. 4** The interpenetration region and the real contact zone

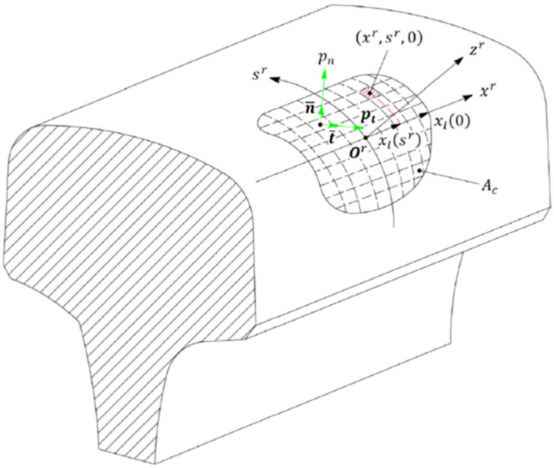


**Fig. 5** Rail contact patch reference system with curvilinear abscissa [3]

As shown in Fig. 5, $s^r$ is the curvilinear abscissa of the rail profile. Therefore, the equation of the new influence function can be written as:

$$w\left(x^r, s^r\right) = \frac{\nu+1}{\pi E} \int_{A_c} \left( \frac{p_n\left(x^{r'}, s^{r'}\right) \cdot \cos(\alpha)(1-\nu)}{\sqrt{\left(x^r - x^{r'}\right)^2 + \left(s^r - s^{r'}\right)^2}} + \frac{p_n\left(x^{r'}, s^{r'}\right) \cdot \sin(\alpha) \cdot K \cdot s^r}{\left(x - x^{r'}\right)^2 + \left(s^r - s^{r'}\right)^2} \right) dA_c \tag{5}$$

According to Kik-Piotrowski's procedure [17], the new influence function has been used to evaluate the normal contact pressure $p_n$ between wheel and rail assuming that:

- The sum of displacement in the geometrical contact point is equal to the rigid penetration:

$$2w(0,0) = \delta \tag{6}$$

- The maximum pressure $p_0$ is known and it is possible to assume a semi-elliptical pressure distribution:

**Fig. 6** FASTSIM contact patch SDEC

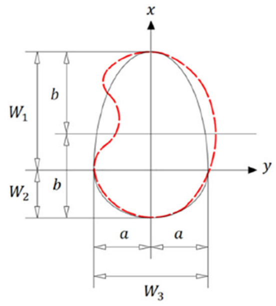


$$p_n\left(x^r, s^r\right) = \frac{p_0}{x_l^r\left(0\right)}\sqrt{x_l^{r2} s^r) - x^{r2}} \tag{7}$$

In this way, the rigid penetration $\delta$ is known, consequently it is possible to evaluate the maximum normal pressure $p_0$ in presence of conformity conditions:

$$\begin{aligned} p_0 = \frac{\pi E P_r x_l^r(0)}{2\left(1+\nu\right)} & \left(\int_{A_c}\left(\frac{\sqrt{x^r\left(s^r\right)^2 - x^{r2}} \cdot \cos(\alpha) \cdot (1-\nu)}{\sqrt{x^{r2}+s^{r2}}}\right.\right. \\ & \left.\left. + \frac{\sqrt{x^{r2}(s^r) - x^{r2}} \cdot \sin(\alpha) \cdot K \cdot s^r}{x^{r2}+s^{r2}}\right) dA_c\right)^{-1} \end{aligned} \tag{8}$$

More details about procedure can be found in the work of Nencioni L. [3].

## 4.2 Tangential problem

Regarding the tangential problem, as shown by [3], it is used an extension of FASTSIM algorithm [17], based on the Kalker Book of Tables for non-Hertzian model [21, 22], to extend the algorithm even to non-elliptical problems. The idea of the KBTNH algorithm is to bring back the non-elliptical, non-symmetrical and non-planar contact patch to a single double elliptical contact (SDEC), as shown in Fig. 6, that is a patch characterized by two fundamental parameters:

$$\begin{cases} a = \sqrt{\dfrac{A_c}{\pi}\dfrac{W_3}{(W_1+W_2)}} \\ b = \sqrt{\dfrac{A_c}{\pi}\dfrac{(W_1+W_2)}{W_3}} \end{cases}$$

In the FASTSIM algorithm it is fundamental the discretization of the contact patches using a grid (Fig. 7), with cell size in longitudinal direction $\Delta x \to \Delta x^r$ and in lateral direction $\Delta y \to \Delta s^r$, the size $\Delta x^r$ of the cell in longitudinal direction is a function of a curvilinear abscissa $s^r$.

After the discretization of the contact patch, the tangential pressure distribution $p_t$ and sliding $s$ calculation is performed. Besides, the normal pressure distribution $p_n$ is known from the normal block of the conformal contact model, as it is shown in the last section. From the FASTSIM algorithm it is possible to evaluate the adhesion pressure $p_A$ in the

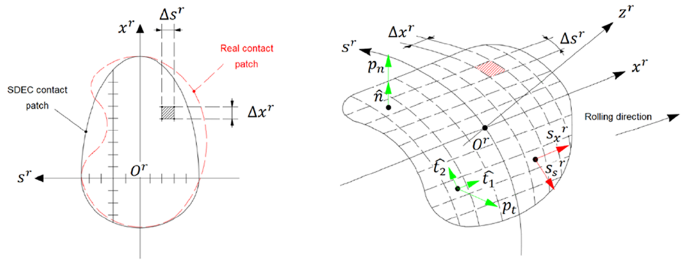


**Fig. 7** Conformal contact patch discretization [3]

node $(x_i^r, s_j^r)$:

$$\boldsymbol{p_A}\left(x_i^r, s_j^r\right) = \boldsymbol{p_t}\left(x_{i-1}^r, s_j^r\right) - \frac{\Delta x^r}{L\left(s^r\right)\overrightarrow{V}}\boldsymbol{S}\left(x^r, s^r\right) \tag{9}$$

Where $L(s^r)$ is the flexibility coefficient, a transfer function obtained from FEM simulations that relates the tangential pressure distributions to the corresponding elastic displacements. It is expressed as a 2 $x$ 2 matrix function of the contact patch coordinates.

The normal pressure $p_n$ in a generic point $(x_i^r, s_j^r)$ of the grid with $1 \le i \le n_{x^r}$, $1 \le j \le n_{s^r}$ is known to form the normal part of the contact problem and it is expressed as follows:

$$\boldsymbol{p_n}\left(x_i^r, s_j^r\right) = p_n\left(x_i^r, s_j^r\right) \cdot \boldsymbol{\hat{n}}\left(s_j^r\right) = \left(\frac{p_0}{x_{il}^r(0)}\sqrt{x_{il}^r\left(s_j^r\right) - x_i^{r2}}\right) \cdot \boldsymbol{\hat{n}}\left(s_j^r\right) \tag{10}$$

Therefore, knowing the first attempt of $p_A\left(x_i^r, s_j^r\right)$ and $p_n\left(x_i^r, s_j^r\right)$ it is possible to calculate the tangential pressure $p_t\left(x_i^r, s_j^r\right)$ and the global local slidings $s(x_i^r, s_j^r)$:

- If $\left\| \boldsymbol{p_A}\left(x_i^r, s_j^r\right)\right\| \le \mu\, p_n\left(x_i^r, s_j^r\right)$ then $\left(x_i^r, s_j^r\right) \in A_{adh}$:

$$\begin{cases} \boldsymbol{p_t}\left(x_i^r, s_j^r\right) = \boldsymbol{p_A}\left(x_i^r, s_j^r\right) \\ \boldsymbol{s}\left(x_i^r, s_j^r\right) = 0 \end{cases} \tag{11}$$

- If $\left\| \boldsymbol{p_A}\left(x_i^r, s_j^r\right)\right\| > \mu\, p_n\left(x_i^r, s_j^r\right)$ then $\left(x_i^r, s_j^r\right) \in A_{sld}$:

$$\begin{cases} \boldsymbol{p_t}\left(x_i^r, s_j^r\right) = \mu p_n\left(x_i^r, s_j^r\right) \cdot \dfrac{\boldsymbol{p_A}\left(x_i^r, s_j^r\right)}{\left\|\boldsymbol{p_A}\left(x_i^r, s_j^r\right)\right\|} \\ \boldsymbol{s}\left(x_i^r, s_j^r\right) = \dfrac{L\overrightarrow{V}}{\Delta x_i^r\left(s_j^r\right)} \cdot \left(\boldsymbol{p_t}\left(x_i^r, s_j^r\right) - \boldsymbol{p_A}\left(x_i^r, s_j^r\right)\right) \end{cases} \tag{12}$$

$A_{adh}$ and $A_{sld}$ are the adhesion and the sliding zones of the contact patch. In conclusion, the distributions of the tangential pressures $p_t\left(x_i^r, s_j^r\right)$ and the local rigid slidings $s(x_i^r, s_j^r)$ are fount iterating the procedure for $2 \le i \le n_{x^r}$, $1 \le j \le n_{s^r}$. As mentioned in the last section, more details about this procedure can be found in the work of Nencioni L. [3].

### 4.3 Conformity index

To quantitatively evaluate the degree of conformity of the wheel–rail contact, an angular conformity index $I_c$ was introduced, defined by the opening angle $\alpha_c$ (Fig. 8) between the

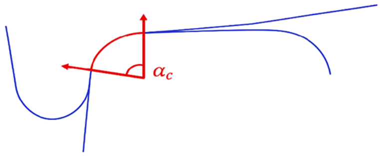


**Fig. 8** Nominal opening angle

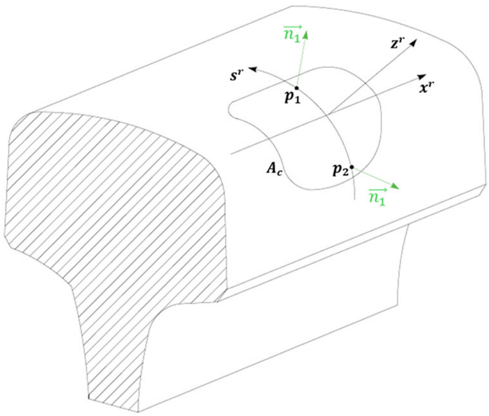


**Fig. 9** Contact patch with local unit vectors and contact points

local tangents to the contacting surfaces. This parameter provides a simple and effective means of discriminating between non-conformal and conformal contact conditions, offering a direct indication of the degree of contact conformity. In particular, the contact is categorized as significantly conformal for $\alpha_c > 18°$.

The opening angle considered for the definition of the conformity index, as shown in Fig. 9, is calculated as follows:

$$\alpha_c = \max \arccos\left[\overrightarrow{n}_1(p_1) \cdot \overrightarrow{n}_2(p_2)\right], p_1, p_2 \in A_c \tag{13}$$

It should be noted that the 18° threshold defined for the conformity index does not represent a strict physical limit for the model's validity, but rather an engineering criterion to identify when conformal corrections become numerically significant. The mathematical formulation presented in Eq. (5) is inherently generalized: as the contact angle $\alpha$ decreases (moving towards the non-conformal regime), the model consistently converges back to the classical Cerruti–Bussinesq's influence function for the elastic half-space. This self-adaptive behavior ensures that the methodology remains robust and physically sound even during the transition between different contact regimes, maintaining the validity of the half-space assumption across a wide range of operational conditions.

The nominal opening angle between the two profiles in the initial configuration is illustrated in Fig. 8 and is approximately 64°. This angle tends to increase as the profiles become more worn, indicating a progressively more conformal contact compared with the initial condition. For instance, in the most critical curves of the track, where the wheel is fully in contact with the rail, the angle $\alpha_c$ increases to a value of approximately 67°. This value corresponds to the simulated wheel profile after a running distance of about 42,785 km, which is the profile later used for the comparison and discussion of the final wear results presented in this study.

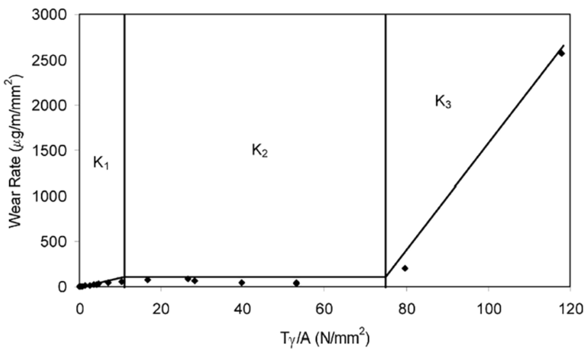


**Fig. 10** Lewis' law provides the relationship between Wear-Index and Wear Rate [25]

## 5 Wear model

In the present work, the selected wear model belongs to the class of energetic approaches based on $T\gamma$ [23]. Such models are generally founded on experimental laws that aim to correlate the dissipated power at the contact, quantified by means Wear Index, with the amount of material removed from the wheel and rail profiles, typically estimated by means Wear Rate [23, 24]. These two parameters are linked through an empirical relationship derived from experimental results obtained with Twin-Disk tests performed under dry conditions. More specifically, as shown in Fig. 10, the experimental relation connects the Wear Rate $K_w$, defined as the mass of removed material per unit contact area ($mm^2$) and per unit of sliding distance ($m$), expressed in $\mu g/(m \cdot mm^2)$, to Wear Index $I_w$, expressed in $N/mm^2$. The Wear Index, which represents the dissipated power generated by the tangential contact pressures, knowing local contact stresses $p_t$ and creepages $s$, can be calculated at each point of the contact patch from the outputs provided by FASTSIM as follows:

$$I_w\left(x_i, y_j\right) = \frac{p_t\left(x_i, y_j\right) \cdot s\left(x_i, y_j\right)}{V} = p_t\left(x_i, y_j\right) \cdot \gamma\left(x_i, y_j\right) \tag{14}$$

where $\gamma$ is creepages and V is the longitudinal vehicle speed.

The experimental relationship, the Lewis's law [23], between $K_w$ and $I_w$ adopted for the wear model is:

$$K_w\left(I_w\right) = \begin{cases} 5.3 \cdot I_w & I_w < 10.4 \\ 55.1 & 10.4 < I_w < 77.2 \\ 61.9 \cdot I_w - 4778.7 & I_w > 77.2 \end{cases} \tag{15}$$

An important aspect is that the dissipated power, estimated through the Wear Index, is experimentally correlated to the mass of material removed per unit surface and unit distance, as measured in bench tests. Consequently, only the fraction of power not converted into heat is effectively considered in the wear evaluation, thus avoiding the risk of overestimation. Once the Wear Index, equivalent for both wheel and rail sides, is known, the corresponding Wear Rate can be determined. Therefore, by introducing the material density, the specific volume of material removed f per unit contact area and distance can be evaluated:

$$\delta_{p^j wi(t)}\left(x_i, y_j\right) = K_{w_w}\left(I_w\left(x_i, y_j\right)\right) \cdot \frac{1}{\rho} \tag{16}$$

$$\delta_{p^j ri(t)}\left(x_i, y_j\right) = K_{w_r}\left(I_w\left(x_i, y_j\right)\right) \cdot \frac{1}{\rho} \tag{17}$$

It should be noted that the wear coefficients used in this study were derived from experimental Twin-Disk tests conducted under dry conditions. The authors acknowledge that environmental factors, such as the presence of moisture, lubricants (oil, water, grease and dust), and other contaminants, as well as the temperature at the contact interface, can influence the wear rate. Consequently, it is important to emphasize that when applying the proposed model to railway characterized by widespread lubrication, friction modifiers, or wet operating conditions, the predicted wear amounts may deviate from actual on-track values. However, the dry condition was selected as it represents a conservative worst-case scenario, providing a safety-oriented baseline for wheel profile evolution and maintenance scheduling. The integration of complex wear maps accounting for variable lubrication conditions and thermal effects is a promising area for future enhancements of the current model.

## 6 Profile update strategy

This section summarizes the profile update strategy, for a full description of this strategy, it is possible to refer to the works available in literature [26, 27].

After evaluating the amount of worn material, the wheel and rail profiles must be updated in order to serve as inputs for the following iteration of the process. The updating procedure involves both integration and averaging steps, aimed at filtering the numerical noise present in the distributions $\delta_{pj(t)}(x, j)$ and at determining the overall material removal due to wear $\Delta^w(s_w)$, $\Delta^r(s_r)$ (in $mm$), where $s_w$ and $s_r$ represent the natural abscissas of the wheel and rail profiles, respectively:

1. Integration in the longitudinal direction of all local wear contributions inside the contact patch, followed by averaging over the full longitudinal extent of both wheel and rail.
2. Time integration of the wear contributions provided by the dynamic simulations, summing over all identified contact points.
3. Accumulation of contributions from left and right wheel-rail pairs to obtain the total rail wear (this step is not required in the case of the wheel).

Since measurable wear typically requires travelled distances of the order of thousands of kilometres, a scaling procedure is adopted to artificially amplify to removed material during the simulation. This makes it possible to reduce the equivalent simulated track length, and consequently the overall computational cost.

To ensure the numerical stability of the iterative process and to maintain a consistent evolution of the contact geometry, the scaling factor used for the profile update is not kept constant. Instead, it is calibrated at each step to ensure that the maximum local wear depth does not exceed 0.4 mm. This threshold represents a robust compromise between computational effort and simulation accuracy, ensuring that the geometric changes between two consecutive updates do not introduce significant variations in the wheel-rail interaction dynamics.

Subsequently, a smoothing operation is applied to the wear functions, in order to mitigate residual numerical oscillations. The update profiles $w_n(s_w)$ and $r_n(s_r)$ are then obtained by removing the smoothed worn material along the normal directions to the original wheel and rail profiles $w_0(s_w)$ and $r_0(s_r)$. Since the removal of material occurs in the normal direction ($n_w^r$ and $n_r^r$, respectively, for wheel and rail), a reparameterization of the resulting profiles is finally required to restore a consistent description in terms of the curvilinear abscissa:

$$\begin{pmatrix} y_w(s_w) \\ w_0(s_w) \end{pmatrix} - \Delta_{sm}^{wsc}(s_w) \cdot \boldsymbol{n_w^r} \rightarrow \begin{pmatrix} y_w(s_w) \\ w_n(s_w) \end{pmatrix} \tag{18}$$

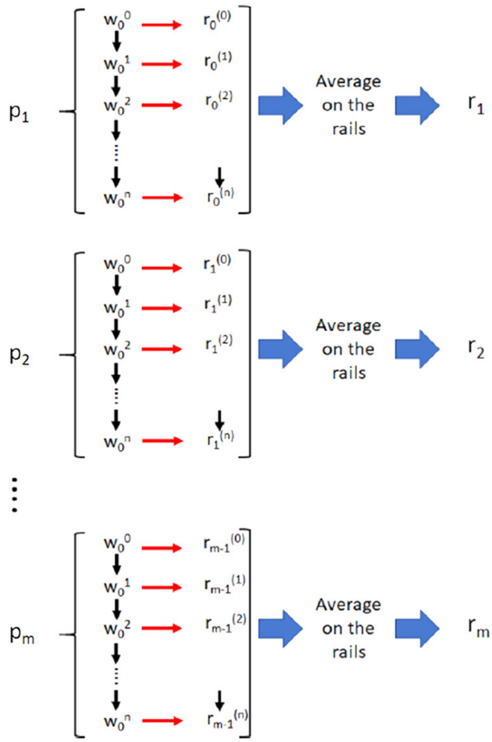


**Fig. 11** Iterative process of profile update strategy

$$\begin{pmatrix} y_r(s_r) \\ r_0(s_r) \end{pmatrix} - \Delta^{rsc}_{sm}(s_r) \cdot \boldsymbol{n}^r_r \rightarrow \begin{pmatrix} y_r(s_r) \\ r_n(s_r) \end{pmatrix} \tag{19}$$

Due to different orders of magnitude involved, the wear evolution of the wheel and rail has been decoupled. Specifically, while wheel wear evolves continuously, the rail profile is assumed to remain unchanged within the considered time window, as its variation is negligible. However, each discrete rail profile interacts, with the same frequency, with all possible wheel profiles.

For this reason, for each rail profile, the wheel wear evolution (from the initial unworn profile to the final worn profile) is simulated. In the first discrete rail step $p_1$, the wheel starting from its initial profile $w_0$ evolves on the unworn rail profile $r_0$, leading to the sequence of worn wheel profile $w_0^1, w_0^2, \ldots, w_0^n$. Each of these wheel profiles is then coupled with the original rail profile $r_0$ to generate a set of virtual rail profiles $(r_0^1, r_0^2, \ldots)$. These are subsequently averaged to define an updated rail profile $r_1$, which is used as the input for the next discrete step.

This iterative process can be repeated $m$ times to perform all the rail steps, as shown in Fig. 11 [28].

## 7 Wear model validation

In order to validate the wheel-side wear model, obtained after implementing the wear laws defined in the previous into the existing framework, a comparison was carried out between

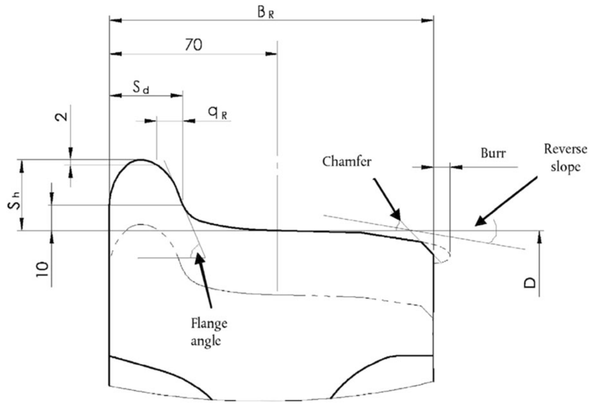


**Fig. 12** Rail wheel reference parameters

the model results, in terms of characteristics dimension and profile geometry, and the experimental wheel profiles measured in service using the Calipri device. As mentioned earlier, in the multibody model developed in Simpack, the actual wheel profiles of the reference vehicle, acquired through direct geometric measurements, were implemented. The data acquisition performed with the Calipri system available at the metropolitan depots of some lines, provided not only the wheel profile geometry but also other relevant parameters, such as the rolling diameter, flange thickness and back-to-back distance.

Despite the large amount the experimental data collected, the validation of the wheel-side model was conducted by comparing the characteristics dimensions of the simulated and experimental profiles. In particular, three fundamental characteristics dimensions were considered (Fig. 12), as they allow the assessment of the wear state of a given profile without the need to reconstruct its full geometry. These three parameters are:

- Flange Thickness (FT): measured horizontally as the distance between the gauge face of the wheel and a point on the profile located 10 mm below the nominal rolling circle, itself positioned 70 mm from the gauge face. This parameter is fundamental, as it provides essential information about the wear state of the active side of the flange.
- Flange Height (FH): measured vertically between the flange tip and the nominal rolling circle. This is another key parameter, as it not only represents the height of the flange, but also provides information on the hollowing of the tread. Indeed, while the flange tip maintains a constant height throughout the profile evolution under wear, point A (defined 70 mm from the gauge face) shifts upward as tread hollowing progresses. Consequently, during profile evolution, the flange height tends to increase.
- QR dimension: measured horizontally between a point on the active side of the flange located 2 mm below the flange tip, and a second point located 10 mm below the nominal rolling circle. This dimension is critical for assessing the wear state of the flange's active side. Generally, if wear is predominant on the flange side rather than on the tread, the QR value decreases.

As can also be observed in Table 2, directly extracted from the experimental measurement reports, threshold limits are defined, both upper and lower, for the characteristic profile parameters, which, for safety purposes, must not be exceeded. In fact, the evolution of these parameters, and particularly wheel wear, can lead, as mentioned in the introduction, to significant modifications of the vehicle's dynamic behavior, such as a reduction of the critical hunting speed. For this reason, knowledge of these parameters, as well as maintaining their values as far as possible from the prescribed limits, is of fundamental importance.

**Table 2** Upper and lower limits of the main wheel profile

| Quote | New [mm] | Limit [mm] |
|---|---|---|
| $Sh$ | 28 | $< 36$ |
| $Sd$ | 31 | $> 20$ |
| $Qr$ | | $6.5 \leq Qr \leq 11.5$ |

The validation was performed on the first wheelset of the vehicle, since it is the one that first interacts with the track and thus also the first to encounter potential contaminants, such as water or oil left by flange lubricators of preceding vehicles. Subsequent wheelsets may not experience contaminations at the interface, due to the removal effect induced by the high-power dissipation at the contact in cases of friction saturation.

The validation process presented in this study focused on the left wheel of the leading axle. This choice is specifically motivated by the track layout of the considered metropolitan line. In the considered travel direction, the layout features a predominance of curves that induce more severe wear conditions of the left wheels. Consequently, under these specific operational conditions, the left wheel represents the most critical and relevant component for an initial assessment of the conformal model's performance. Therefore, for the purposes of this preliminary study, focusing on the left wheel is considered sufficient to demonstrate the model's accuracy and its ability to handle high conformity contact conditions.

The rail profile adopted in the simulations corresponds to a UIC 50 section. Since the rail is not the focus of this study, its wear behavior was not analysed in detail. Therefore, the temporal evolution of rail profile wear was not considered; instead, a representative worn profile was assumed as constant throughout the analyses. Figure 13 shows the worn rail profile used in the simulations. This reference profile was obtained from field measurements conducted during experimental campaigns on the reference curve, which was identified as one of the most critical sections of the track in terms of wear severity. The monitoring of the rail geometry covered the operational tracking period of the experimental campaign. Within this observed timeframe, the experimental data indicated that the rail profile did not exhibit significant or measurable wear degradation. Consequently, keeping this representative worn rail profile constant throughout the simulation constitutes a reasonable and experimentally validated assumption for the simulated operational cycle, although long-term deviations will be subject to future modeling enhancements.

As previously mentioned, the test case considered in this study refers to an Italian metro line. Figure 14 shows the layout of the track on which the simulations were performed.

## 8 Wear model results

The results refer to the first wheelset of the vehicle, since it is the first to interact with the track and therefore the most susceptible to environmental contaminants, such as water or oil residues left by the flange lubricators of preceding rolling stock. The subsequent wheelsets may not experience the presence of contaminants at the wheel–rail interface, due to the contaminant removal effect induced by the high-power dissipation at the contact, particularly under conditions where the friction limit is saturated. Furthermore, Fig. 15 shows the initial wheel profile implemented in the multibody vehicle models, corresponding to the profile measured in service using the Calipri device.

Regarding the numerical simulation, in accordance with the profile updating and scaling procedure discussed previously, the maximum material removal per step from the wheel

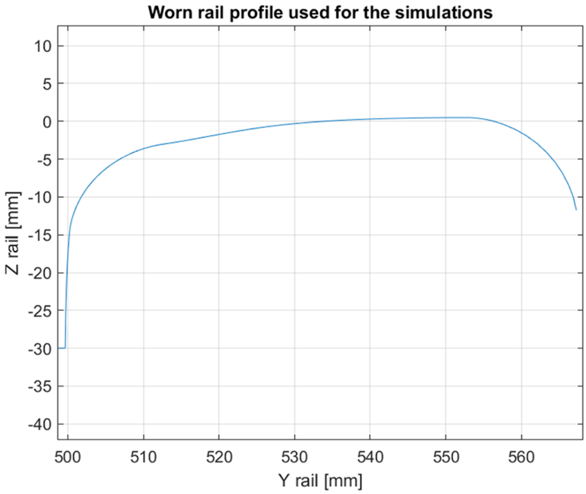


**Fig. 13** Worn rail profiles used for the simulations

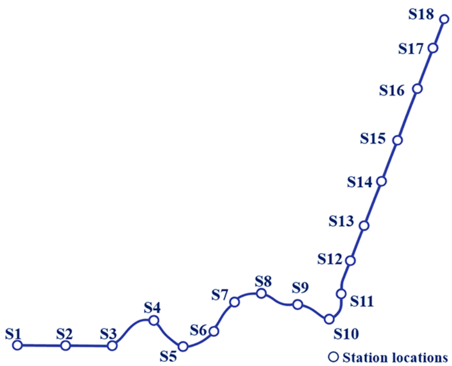


**Fig. 14** Layout of the track

profile was set to 0.4 mm. By assuming this value, the model continues to simulate wear until the profile reaches the prescribed depth of 0.4 mm, after which it proceeds to the next discrete simulation step.

Figure 16 shows the evolution of the wheel profile, in conditions of conformal contact, each simulation step obtained from the numerical analyses. Figures 17 and 18 present enlarged views of the wheel regions most affected by wear, that are the wheel tread and the flange. Some considerations can be made regarding the wear mechanisms of the profiles. It can be observed that, compared with the flange, where wear mechanisms are present but lead to negligible material loss, the depression on the wheel tread is more pronounced. This indicates that the contact during most of the operation is predominantly located on the tread rather than on the active face of the flange. Such behavior is mainly due to the geometry of the test-case track, which is largely straight. Consequently, contact on the flange face is absent except for a single curved section of the track, which is responsible for the slight wear observed on the wheel flange.

After a total running distance of 49,905 km, the wheel profile shows a tread wear depth of 2.784 mm and a flange wear depth of 0.78 mm.

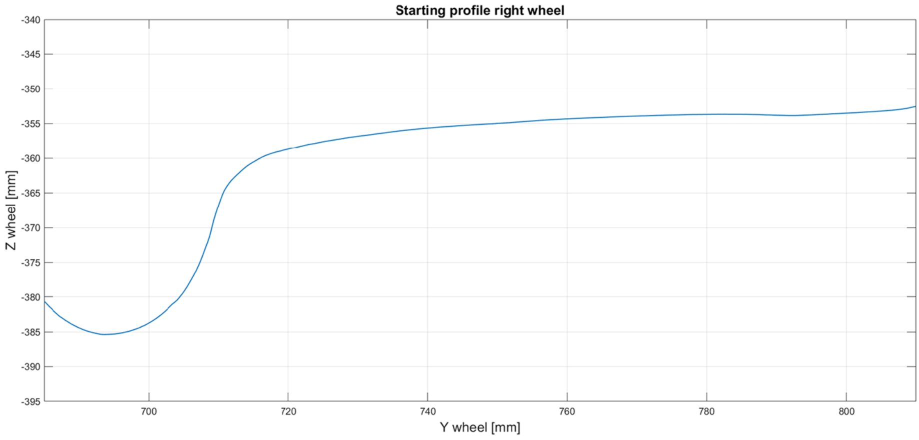


**Fig. 15** Starting profile right wheel

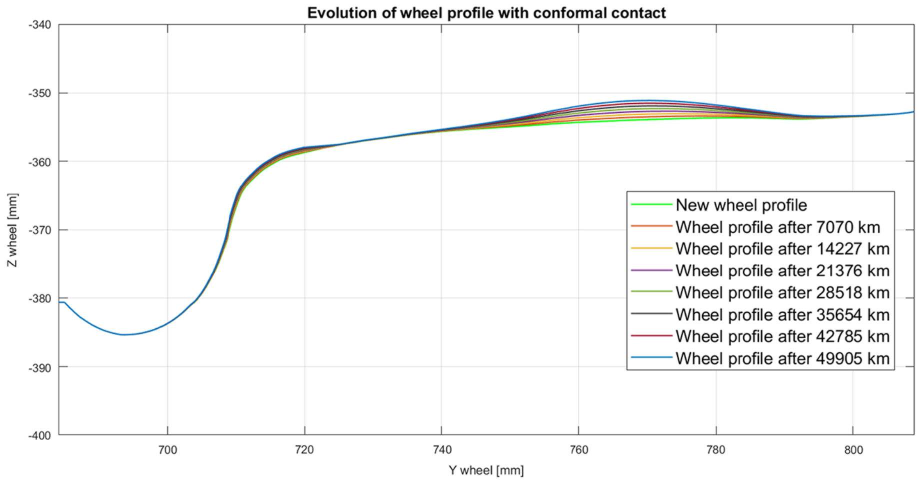


**Fig. 16** Evolution of wheel profile with conformal contact

Figure 19 shows the evolution of wheel profile, in conditions of non-conformal contact, while Fig. 20 and Fig. 21 show detailed views of the wheel areas most affected by wear, that are the wheel tread and the flange.

In the case of non-conformal contact, the wear values measured on the wheel tread and flange are 2.782 mm and 0.5 mm, respectively. Compared with the conformal contact case, the total simulated running distance at the end of the seven wear steps amounts to 73,287 km. This result highlights that the conformal contact model tends to overestimate wear with respect to the non-conformal contact model. The overprediction can be attributed to the larger and more persistent contact area assumed in the conformal contact case, which leads to higher contact stresses and higher contact pressure and, consequently, a greater amount of material removal during the wear evolution.

Given the simulated wheel profiles and the discretized coordinates, it is possible to represent the characteristic geometric parameters of the wheel profile (Qr, Sd, and Sh) as a

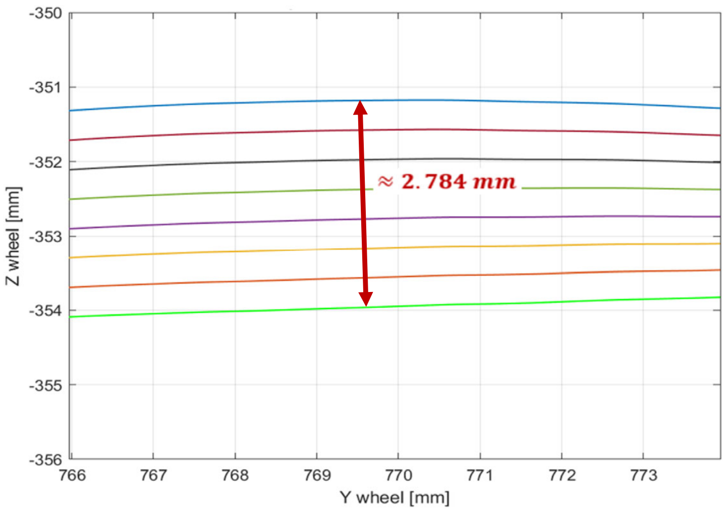


**Fig. 17** Evolution of wheel profile with conformal contact; zoom on the wheel tread

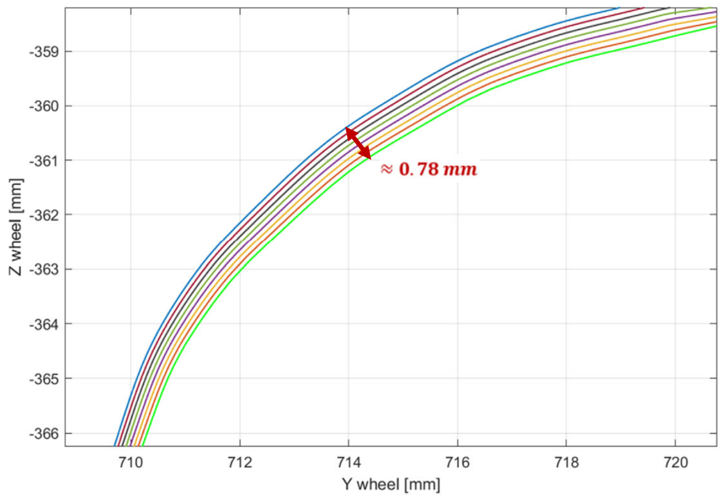


**Fig. 18** Evolution of wheel profile with conformal contact; zoom on the wheel flange

function of the travelled distance. In Figs. 22, 23 and 24 are shown the comparison of the evolution of these parameters with running distance for both conformal and non-conformal contact cases. From these trends, it can be observed that both the flange thickness and flange height increase in both the conformal and non-conformal contact cases. It is possible to see that in the conformal contact conditions, these parameters exhibit a faster growth rate. Regarding the Qr dimension, in the conformal case it tends to decrease with increasing running distance, while in the non-conformal case an opposite trend is observed, with Qr progressively increasing. This behavior can be explained by the different contact conditions characterizing the two models. The increase in flange height and thickness results from the predominant wear occurring on the wheel tread, which lowers the rolling circle level, con-

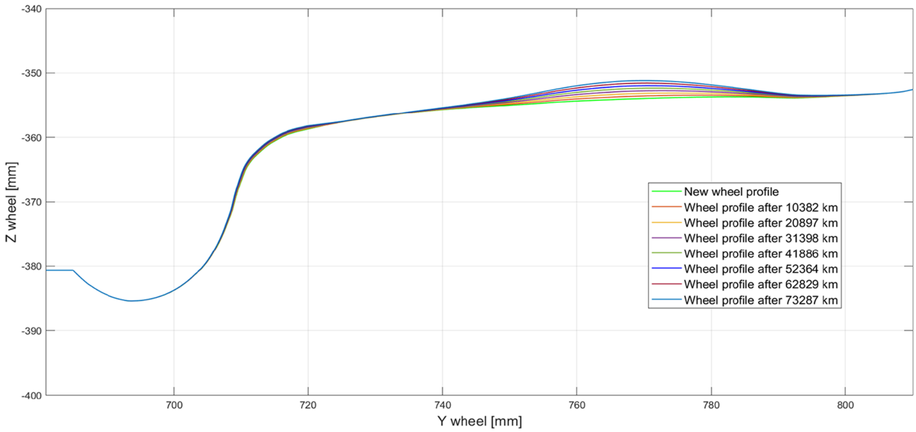


**Fig. 19** Evolution of wheel profile with non-conformal contact

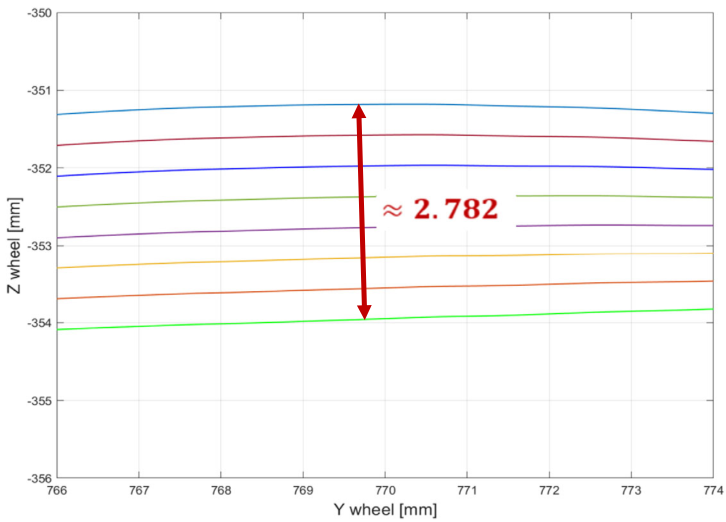


**Fig. 20** Evolution of wheel profile with non-conformal contact; zoom on the wheel tread

sequently altering the reference points used to determine the flange dimensions. The more pronounced growth of these parameters in conformal contact is due to the larger and more persistent contact area, which produces higher wear rates on the tread. In conformal case, the reduction of Qr dimension indicates a shift of the wheel–rail contact area toward the flange root, occurring when material removal in that region becomes significant, while in the non-conformal contact case the smaller and more localized contact area maintains the contact closer to the nominal rolling circle, leading to a slight increase in Qr.

In Fig. 25, a comparison is presented between the wheel profiles obtained under conformal and non-conformal contact conditions, together with the experimental profile measured for a similar running distance. The conformal and non-conformal profiles correspond to different simulation steps: specifically, step 6 for the conformal contact case (42,785 km) and step 4 for the non-conformal contact case (41,886 km).

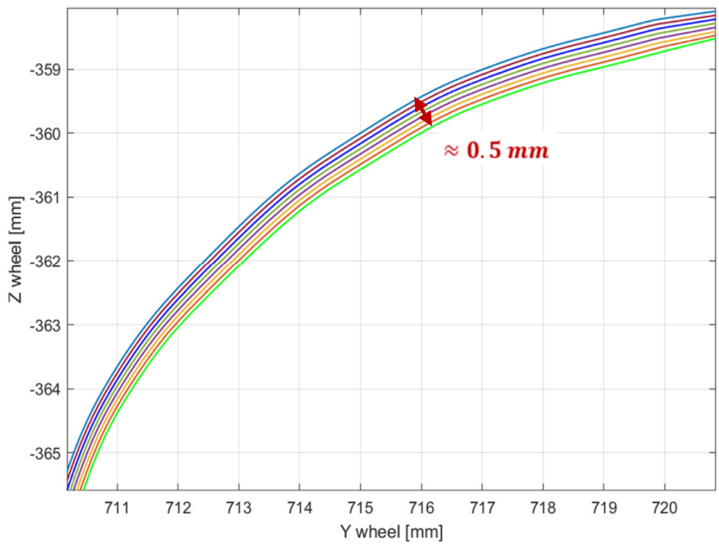


Fig. 21 Evolution of wheel profile with non-conformal contact, zoom on the wheel flange

Fig. 22 Comparison of Qr evolution for conformal and non-conformal contact cases

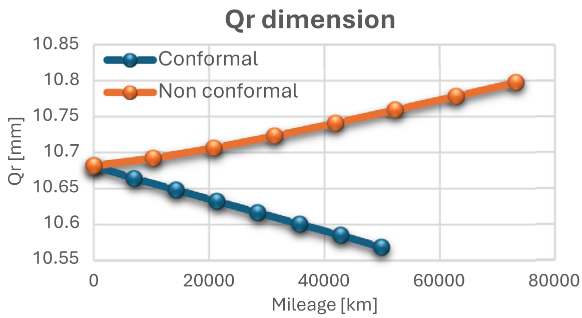


Fig. 23 Comparison of Flange thickness Sd for conformal contact and non-conformal contact cases

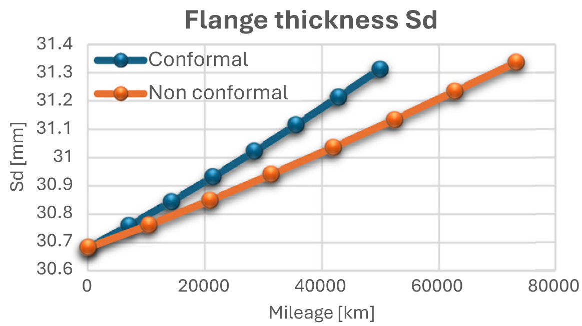


Although the experimental profile does not perfectly coincide with the one predicted by the conformal contact model, this can be interpreted as further evidence of the higher reliability of the proposed approach. The measured profile reflects complex and variable operating conditions, such as contamination, microslips, thermal variations, and geometric

**Fig. 24** Comparison of Flange height Sh for conformal contact and non-conformal contact cases

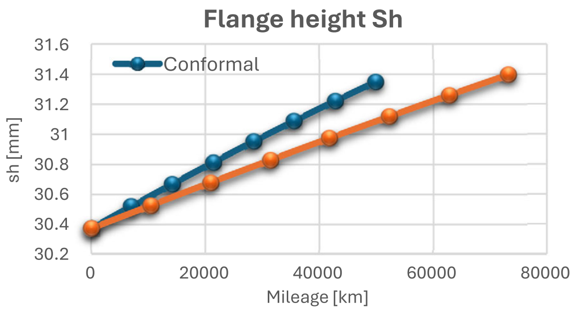


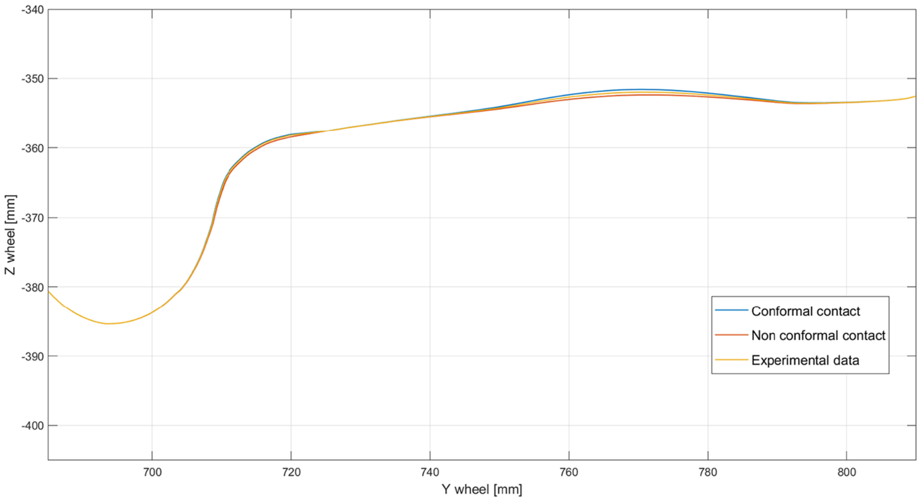


**Fig. 25** Comparison between the wheel profiles obtained at step 6 of conformal contact, step 4 of non-conformal contact and experimental data

tolerances, that cannot be fully reproduced in numerical simulations. Within this context, the conformal contact model captures the contact and wear dynamics with greater consistency, providing results that are significantly closer to the real behavior of the wheel-rail system. The remaining discrepancy, mainly observed in the enlarged view of the wheel tread, suggests possible directions for future model improvements. Nevertheless, it does not compromise the validity of the model; rather, it highlights its ability to represent the physical mechanisms of wear evolution in a more realistic and robust manner compared to traditional approaches

The experimental profile, obtained from measurements at a comparable running distance, closely matches the one predicted by the conformal contact model, confirming the higher reliability and predictive capability of the approach proposed in this work.

By observing the differences between the conformal and non-conformal contact profiles, these results are consistent with the trends previously noted for the characteristic parameters (Qr, Sd, and Sh). The conformal contact model tends to overestimate wear compared with the non-conformal model, due to the higher contact pressures generated under conformal contact conditions, which lead to a significantly greater amount of material removal.

Figure 26 provides an enlarged view of the wheel tread regions, revealing the differences between the two profiles. As previously discussed, the profile obtained under conformal

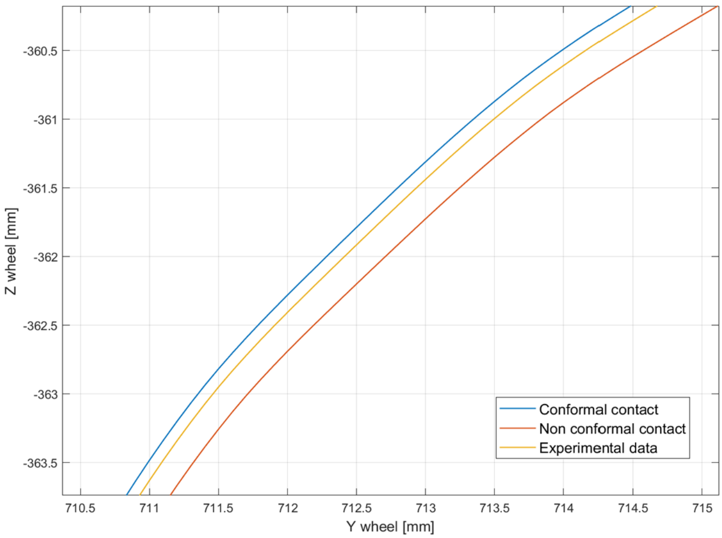


**Fig. 26** Comparison between the wheel profiles obtained at step 6 of conformal contact, step 4 of non-conformal contact and experimental data, zoom on the wheel flange

contact conditions exhibits more pronounced wear. The figure also shows the difference in material removal between the two profiles, with $\delta_{flange} \approx 0.345\ mm$.

The robustness of the proposed methodology is demonstrated by the high degree of numerical stability maintained throughout the entire wear evolution process. The algorithm is specifically tuned to handle the transition between different contact conditions without inducing discontinuities in the contact forces or kinematic oscillations. This ensures that even as the wheel profile geometry evolves significantly through the 7 calculation steps, the multibody solver maintains excellent convergence rates. Regarding parameter sensitivity, the model was configured using standard values for the friction coefficient and material properties, which are consistent with the metropolitan operational context. It should be emphasized that the primary focus of this work is the formulation and validation of the conformal modelling approach. A systematic parameter sensitivity analysis (such as variations of the friction coefficient, or material elastic moduli) constitutes a separate and extensive research task and will be carried out in future work.

Nevertheless, the consistency of the results confirms that the model is well-posed and that the integration between the conformal contact formulation and the dynamic solver is insensitive to minor numerical perturbations, providing a reliable baseline for long-term wear predictions.

To perform a quantitative evaluation of the model's performance, a comparison within the conformal and non-conformal contact models has been carried out. The numerical simulations were managed on a workstation equipped with an Intel® Core ™ i9-13900K 3.00 GHz and 128 GB of RAM. As shown in Table 3, the computational time required for the complete multi-step wear simulation is approximately 5 hours for both the conformal and non-conformal contact models. These data demonstrate that the integration of the extended Kik-Piotrowski and enhanced FASTSIM algorithms provides superior physical insights into the wheel-rail interface without any additional computational penalty compared to the simplified Hertzian contact models.

**Table 3** Computational performance and simulation parameters

| Parameter | Non- conformal contact | Conformal contact | Implementation software |
|---|---|---|---|
| Number of wear steps | 7 | 7 | MATLAB – Simulink / Simpack |
| Total simulation time | 5 h | 5 h | MATLAB – Simulink / Simpack |

## 9 Conclusion

In conclusion, wear represents one of the main mechanisms affecting the life of railway wheels. Therefore, understanding and predicting wheel-rail wear is fundamental not only for the definition of effective maintenance strategies but also for ensuring safe vehicle operation throughout its service life. Most of the models available in literature describing the wheel-rail contact are based on the simplifying assumption of non-conformal contact, where the contact patch is much smaller than the dimension of the contacting bodies. In this study, by contrast, a conformal contact approach was adopted. This condition occurs when the contact area is not negligible compared with the curvature radii of wheel and rail, and thus the contact patch takes on a curvilinear shape.

The numerical results, obtained through co-simulation between Simpack and MATLAB/Simulink, demonstrate the effectiveness of the interaction between the wear model and the multibody vehicle model, applied to a test case representative of an Italian metropolitan scenario. The analysis shows that, while both models predict comparable global wear trends in the considered scenario, the conformal contact model provides a more detailed and consistent description of the wear distribution along the wheel profile. Specifically, the proposed approach better captures the evolution of the profile shape in high conformity zones, such as the flange and the root area. These results highlight that while traditional models may provide a reasonable approximation in some cases, the conformal approach proves to be a more robust tool for scenarios where profile evolution leads to highly conformal interactions, where Hertzian assumptions typically lose validity.

Despite the promising results, the current study presents some limitations. The rail profile was assumed to remain unchanged, neglecting the concurrent wear evolution of the rail geometry. As demonstrated by Ignesti et al. [27] within a coupled wear framework, assuming a fixed, nominal rail profile artificially concentrates the wheel-rail contact points in a narrower band. Because the mutual geometric adaptation of the two interacting profiles is neglected, this uncoupled approach typically leads to a localized overestimation of the maximum wheel wear depth (often in the range of 10% for long-term predictions) since the contact pressures are not realistically distributed over a widening area. Consequently, future research will be specifically focused on the development of a dedicated rail wear model. This advancement will be integrated with the current wheel wear model to enable fully bidirectional interaction, resulting in a more effective and realistic simulation of the wheel-rail system. This model will allow for the simultaneous assessment of both wheel and rail wear evolution under conformal contact conditions, significantly enhancing predictive accuracy by accounting for the mutual and continuous geometric interaction of both profiles.

In addition to this methodological development, future outlook will focus on two further key aspects to enhance the model's comprehensiveness. While the current study focused on the left wheel as the most critically stressed component for the analyzed metropolitan scenario, extending the model to include the right wheels and all vehicle axles remains a priority. This expansion, accounting for bidirectional travel and varying track configurations, will provide a complete representation of the wear evolution for all the vehicle wheelsets.

Furthermore, to fully demonstrate the numerical robustness and generality of the proposed formulation, future investigations will address more complex operational scenarios that go beyond the current test case. This includes the validation of the model under high-curvature conditions, significant gradients and varying loading conditions. Such assessments are essential to confirm the model's performance across the full spectrum of railway applications.

**Author contributions** Conceptualization, methodology, software and validation F. Distaso, L. Nencioni and A. Cascino; review, supervision, project administration E. Meli and A. Rindi. All authors have read and agreed to the published version of the manuscript.

**Funding information** Open access funding provided by Università degli Studi di Firenze within the CRUI-CARE Agreement. This research did not receive any specific grant from funding agencies in the public, commercial, or not-for-profit sectors.

**Data availability** No datasets were generated or analysed during the current study.

## Declarations

**Competing interests** The authors declare no competing interests.



## References

1. Li, Z., Kalker, J.: Simulation of severe wheel-rail wear. In: Proceedings of the 6th International Conference on Computer Aided Design, Manufacture and Operation in the Railway and Other Advanced Mass Transit Systems, Lisbon, Portugal, Sep. 2–4, pp. 393–402 (1998)
2. Butini, E., Marini, L., Meli, E., Panconi, S., Rindi, A., Romani, B.: A new wear model considering wheel-rail conformal contact. In: First International Conference on Rail Transportation 2017, pp. 237–249. American Society of Civil Engineers, Reston (2017)
3. Nencioni, L., Meli, E., Rindi, A., Shi, Z.: A new efficient conformal contact model for multibody and railway applications. Multibody Syst. Dyn. **64**(4), 587–626 (2025)
4. Pombo, J., Ambrósio, J., Silva, M.: A new wheel–rail contact model for railway dynamics. Veh. Syst. Dyn. **45**(2), 165–189 (2007)
5. Marques, F., Magalhães, H., Pombo, J., Ambrosio, J., Flores, P.: A three-dimensional approach for contact detection between realistic wheel and rail surfaces for improved railway dynamic analysis. Mech. Mach. Theory **149**, 103825 (2020)
6. Piotrowski, J., Chollet, H.: Wheel–rail contact models for vehicle system dynamics including multi-point contact. Veh. Syst. Dyn. **43**(6–7), 455–483 (2005)
7. Liu, B., Bruni, S.: Comparison of wheel–rail contact models in the context of multibody system simulation: Hertzian versus non-Hertzian. Veh. Syst. Dyn. **60**(3), 1076–1096 (2022)
8. Yan, W., Fischer, F.D.: Applicability of the Hertz contact theory to rail-wheel contact problems. Arch. Appl. Mech. **70**(4), 255–268 (2000)
9. Vollebregt, E.A.H., Iwnicki, S.D., Xie, G., Shackleton, P.: Assessing the accuracy of different simplified frictional rolling contact algorithms. Veh. Syst. Dyn. **50**(1), 1–17 (2012)
10. Kalker, J.J.: A fast algorithm for the simplified theory of rolling contact. Veh. Syst. Dyn. **11**(1), 1–13 (1982)
11. Hertz, H.: The contact of elastic solids. J. Reine Angew. Math. **92**, 156–171 (1881)

12. Kalker, J.J.: Wheel-rail rolling contact theory. Wear **144**(1–2), 243–261 (1991)
13. Kalker, J.: The computation of three-dimensional rolling contact with dry friction. Int. J. Numer. Methods Eng. **14**(9), 1293–1307 (1979)
14. Kalker, J.J.: Users Manual of the Fortran Program CONTACT (1986). Delft University of Technology, Department of Math. and Computer Science, Delft
15. Chen, Y., Liu, B., An, B., Wang, P., Bruni, S.: A fast method for solving conformal rolling contact problems. Veh. Syst. Dyn. **62**(8), 1903–1928 (2024)
16. Chen, Y., Liu, B., Bruni, S.: Assessment of simplified models of conformal wheel-rail rolling contact. In: The IAVSD International Symposium on Dynamics of Vehicles on Roads and Tracks, pp. 577–588. Springer, Cham (2023)
17. Piotrowski, J., Kik, W.: A simplified model of wheel/rail contact mechanics for non-Hertzian problems and its application in rail vehicle dynamic simulations. Veh. Syst. Dyn. **46**(1–2), 27–48 (2008)
18. Blanco-Lorenzo, J., Santamaria, J., Vadillo, E.G., Correa, N.: On the influence of conformity on wheel–rail rolling contact mechanics. Tribol. Int. **103**, 647–667 (2016)
19. Zheng, X., Zhang, J., Xiong, K., Shu, X., Han, L.: Boundary face method for 3D contact problems with non-conforming contact discretization. Eng. Anal. Bound. Elem. **63**, 40–48 (2016)
20. Hashemi, J., Paul, B.: Contact stresses on bodies with arbitrary geometry, applications to wheels and rails (1979). No. MEAM-79-2
21. Piotrowski, J., Liu, B., Bruni, S.: The Kalker book of tables for non-Hertzian contact of wheel and rail. Veh. Syst. Dyn. **55**(6), 875–901 (2017)
22. Kalker, J.J.: Three-Dimensional Elastic Bodies in Rolling Contact. Springer, Berlin (2013)
23. Lewis, R., Dwyer-Joyce, R.S.: Wear mechanisms and transitions in railway wheel steels. Proc. Inst. Mech. Eng., Part J J. Eng. Tribol. **218**(6), 467–478 (2004)
24. Braghin, F., Lewis, R., Dwyer-Joyce, R.S., Bruni, S.: A mathematical model to predict railway wheel profile evolution due to wear. Wear **261**(11–12), 1253–1264 (2006)
25. Lewis, R., Braghin, F., Ward, A., Bruni, S., Dwyer-Joyce, R.S., Bel Knani, K., Bologna, P.: Integrating dynamics and wear modelling to predict railway wheel profile evolution (2003)
26. Innocenti, A., Marini, L., Meli, E., Pallini, G., Rindi, A.: Development of a wear model for the analysis of complex railway networks. Wear **309**(1–2), 174–191 (2014)
27. Ignesti, M., Malvezzi, M., Marini, L., Meli, E., Rindi, A.: Development of a wear model for the prediction of wheel and rail profile evolution in railway systems. Wear **284**, 1–17 (2012)
28. Butini, E., Marini, L., Meacci, M., Meli, E., Rindi, A., Zhao, X.J., Wang, W.J.: An innovative model for the prediction of wheel-rail wear and rolling contact fatigue. Wear **436**, 203025 (2019)